ACS OMEGA

Open Access

http://pubs.acs.org/journal/acsodf

Article

Olive Oil-Based Reverse Microemulsion for Stability and Topical Delivery of Methotrexate: In Vitro

Mohammad Changez,* Mohammad Faiyaz Anwar, and Hilal Alrahbi

Cite This: *ACS Omega* 2024, 9, 7012−7021

Read Online

ACCESS | Metrics & More | Article Recommendations | Supporting Information

ABSTRACT: Hydrolysis of pharmaceutically active molecules can be in control under a confined environment of water-in-oil microemulsion. Stability of model drug methotrexate (MTX) in a sodium bis(2-ethylhexyl) sulfosuccinate (AOT) and olive oil microemulsion system has been evaluated. The physicochemical properties of AOT-MTX-water-olive oil reverse microemulsion (MTX-RM) were examined by UV−vis, Fourier transform infrared, and X-ray diffraction techniques, and the hydrodynamic size was determined by dynamic light scattering techniques and morphologies were characterized by a transmission electron microscope and atomic force microscope. In vitro permeation of MTX-RM through treated skin and its mechanism are evaluated by a UV−visible spectrophotometer, confocal laser scanning microscope, differential scanning calorimeter, and attenuated total reflecting infrared spectroscopy (ATR). The interaction of MTX with the AOT headgroup in confined environment RM enhanced the stability of MTX without affecting the molecular integrity at room temperature. Chemical stability of MTX in MTX-RM (W_0 = 5) is significantly higher (~97%) at room temperature for the study period of 1 year than in MTX-RM (W_0 = 15) (~72%). Interaction of MTX with the AOT headgroup is also visualized by a high-resolution transmission electron microscope and is in correlation with FT-IR data of MTX-RM. The skin fluxes of MTX are 15.1, 19.75, and 22.75 times higher at water content (W_0) of 5, 10, and 15, respectively, in MTX-RM in comparison to aqueous solution of MTX. The enhanced amounts of the MTX were detected using CLSM in hair follicles, sweat glands, and epidermis layer of the skin. Merging of T_2, T_3, and T_4 thermal peaks in one broad peak in treated skin endothermograph shows that carrier MTX-RM affects the lipid as well protein structure of the treated skin. ATR data of treated skin showed an increase in the intensity of the carbonyl peak at 1750 cm^{-1} (lipid), shifting of the amide II peaks, and separation of peaks in the range of 1060 to 1000 cm^{-1} (vibration mode of $-CH_2OH$, C−O stretching, and C−OH bending peak of the carbohydrate) in comparison to control skin, which indicates that MTX-RM interacts with glycolipid and glycoprotein through carbohydrate hydroxy groups.

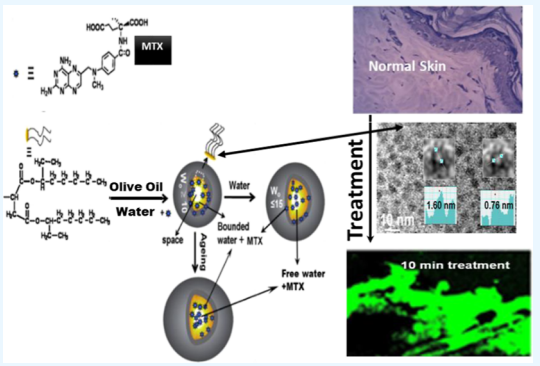

1. INTRODUCTION

Methotrexate (4-amino-10-methyl folic acid or 4-amino-4-deoxy-10-methylpteroyl-L-glutamic acid) (MTX) (Figure 1a) is a well-known folic acid analogue that inhibits thymidylate biosynthesis and purine and thus hinders the synthesis of ribonucleic acid and deoxyribonucleic acid. MTX, as an immunosuppressant drug, was used for the treatment of prophylaxis, cancers, psoriasis, rheumatoid arthritis, and bone marrow transplantation.[1−4] The amide linkages in the MTX molecule are hydrolyzed in aqueous solutions, leading to the formation of glutamic acid and 4-amino-4-deoxy-10-methyl-pteroic acid (Figure 1a). The degradation products of MTX at high doses are cytotoxic against neoplastic cells, causing bone marrow depression, disturbing replicating healthy cells, and producing inflammation in the gastrointestinal tract.[3,5−7] Thus, to avoid or minimize the cytotoxicity of MTX in susceptible normal cells, it is integral to find the proper delivery carrier or strategy that enables the delivery of the optimal concentrations of MTX.

As formulation scientists have focused on the strategies involved with the micro-/nanostructure carriers for numerous pharmaceutical molecules, microemulsion may serve as an efficient carrier for transdermal drug delivery systems.[8−12] Microemulsion has demonstrated enormous advantages over other formulations including hydrogel and liposome-based carrier systems, mainly due to thermodynamic stability, low viscosity, and capability to solubilize hydrophilic as well as hydrophobic molecules.[13−16] Microemulsion is an isotropic mixture (heterogeneous at the micro level) of oil, water, and surfactant (with/without a cosurfactant) and acts as compartments like nano-/microstructure. Therefore, it can be a carrier

Received: November 8, 2023
Revised: December 18, 2023
Accepted: January 17, 2024
Published: February 2, 2024

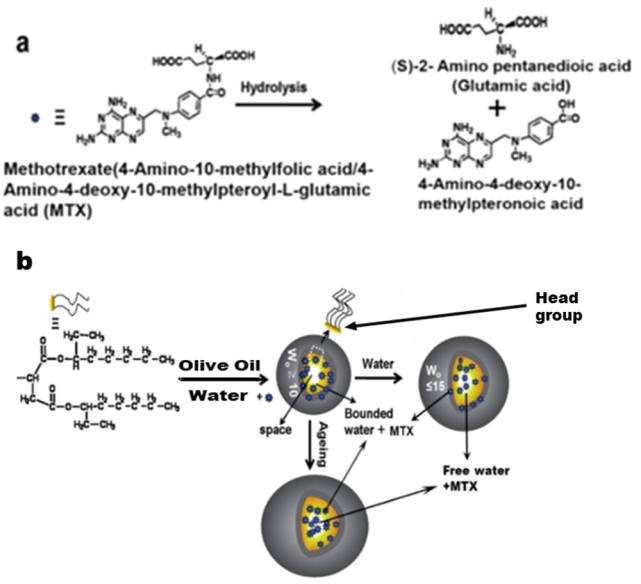

Figure 1. (a) Mechanism for the hydrolysis of MTX and (b) chemical structure of the AOT and formation of the microemulsion.

for hydrophilic as well as hydrophobic pharmaceutically active molecules alone or in combination, and its architecture can be controlled by changing its environmental conditions, temperature, nature of its chemical components, additives, and the amount of water.[17,18]

The delivery of physiochemically unstable molecules subject to the metabolic process is challenging in the development of pharmaceutical dosage forms. Especially, dispersibility and stability issues of drugs including peptides during preparation and storage conditions greatly hamper the broad application of nanocarrier drug delivery systems.[16] The aerosol-OT (AOT) [sodium bis(2-ethylhexyl) sulfosuccinate: Figure 1b] formed cosurfactant-free reverse microemulsion (RM) in nonaqueous solvents.[19] The amount of solubilized water was calculated as a molar ratio of water to AOT (W_0 = [H_2O]/[AOT]). The numerical value of W_0 represents the number of water molecules added per molecule of surfactant and has been considered as an integral parameter in determining the size and shape of the microemulsion droplets.[20,21]

As shown in Figure 1b, the water droplets in the RM are surrounded by the hydrophilic group of surfactants. The chemical nature and shape of the water droplet in the inner core of RM need to be characterized for determining proper loading doses and maintenance of the stability of pharmaceutical molecules.[22]

In this study, for efficient topical delivery of MTX, RM has been explored as the carrier for the MTX. Considering the toxicity of MTX at high concentrations and susceptibility to thermal and chemical degradation, the confinement effects of the W/O RM approach on the stability of MTX in the AOT-MTX-water−olive oil reverse microemulsion (MTX-RM). The olive oil (OL) is selected because it is a preferred oil worldwide for food applications and belongs to the monounsaturated fatty acids group, which lowers total cholesterol and low-density lipoprotein levels and prevents blood clotting.[23,24]

The physicochemical properties of the RM was characterized using various analytical methods, such as nuclear magnetic resonance, small-angle X-ray scattering, and terahertz spectroscopy.[25−29] The presence of MTX in AOT-MTX-water−OL reverse microemulsion enhanced contrast without adding any staining agent and was detected by a transmission electron microscope. The thin film X-ray diffraction (XRD) analysis was used for identifying the molecular integrity of MTX in MTX-RM. The permeation profiles of MTX through the treated skin were also evaluated at hair follicles, sweat glands, and the epidermis layer of the mouse skin. Cytotoxicity of the formulation was evaluated by the MTT test on melanoma cell B10−F16. The RM system was optimized as a stabilizing carrier for MTX, which is unstable due to the hydrolysis process.

2. EXPERIMENTAL SECTION

2.1. Materials. MTX (Mw 454.4), aerosol-OT [AOT, i.e., sodium bis(2-ethylhexyl)] sulfosuccinate (Mw 444.44), and fluorescein isothiocyanate (FITC) were purchased from Sigma. Extra virgin olive oil (from local super market), ethanol (sd-Fine), and high-performance liquid chromatography (HPLC) grade water (Merck) were used without further purification for preparation of the AOT-methotrexate-water-OL RM.

2.2. Preparation and Characterizations of Microemulsion. The scheme for the preparation of the AOT-methotrexate-water−OL RM (MTX-RM) is depicted in Figure 1b. In brief, 44.44 mg of AOT was dissolved in 1.00 mL of OL to make a 0.1 M AOT solution. RM was prepared at W_0 = 5, 10, 15, and 20 by adding the proper amount of water, respectively, and subsequently adding MTX solution to make constant loading concentrations, as shown in Table 1. MTX is soluble in HPLC-grade water at a slightly basic pH of 7.4, which was adjusted by the addition of 0.001N NaOH. Initially, an addition of MTX solution in water produced slight turbidity; however, once water droplets containing MTX were solubilized after sonication, the system became transparent.

2.3. Hydrodynamic Size and Zeta Potential. Dynamic light scattering is a technique in physics that can be used to determine the size distribution profile of small particles in a suspension in solution. The Zetasizer Ver. 6.01, Malvern instrument was used to determine the size distribution profile and zeta potential of AOT-MTX-water−OL Reverse Micelles with and without MTX at different W_0 were placed in clear disposable zeta cells, and results were recorded.

2.4. Stability of Methotrexate in AOT-Methotrexate-Water−Olive Oil Reverse Microemulsion. The chemical

Table 1. Composition of AOT-Methotrexate (MTX)-Water−OL RM and Zeta Potential

concentration of AOT	W_0 = [H_2O]/[AOT]	concentration of MTX in RM (μg/mL)	average zeta potential before MTX loading (mV)	average zeta potential after MTX loading (mV)
0.1 M	5	400	−29.42	−26.30
0.1 M	10	400	−29.94	−27.65
0.1 M	15	400	−34.28	−31.44
0.1 M	20	400	−35.54	−32.16

https://doi.org/10.1021/acsomega.3c08875
ACS Omega 2024, 9, 7012−7021

stability of MTX in RM was monitored by UV−vis (Win-Carry 100) and Fourier transform infrared (FT-IR) (PerkinElmer) spectrophotometers using the KBr liquid cell over a frequency range of 4000−400 cm^{-1}. A UV−Vis spectrophotometer (CARY 1E) scan was carried out for pure MTX solution and AOT-water−OL RM with or without MTX in the wavelength range of 200−800 nm. The standard curve of the MTX was prepared by recording the absorbance at 302 nm, and its stability in RM was also monitored at the same wavelength. The status of molecular conformations and crystal packing of pure MTX and MTX in MTX-RM was compared by measurement of thin-film XRD on a silica substrate using a Rigaku-X-ray diffractometer equipped with RINT2000 wide-angle goniometer (40 kV/40 mA at scan rate 1.2°/min, copper as an anode).

2.5. Morphology Analysis of Reverse Microemulsion by a Transmission Electron Microscope. For the morphological study, an energy-filtering transmission electron microscope [EM 912 OMEGA (ZEISS, S-4700), 120 kV] was used. For the preparation of TEM specimens, the solutions were drop-cast on carbon-coated copper grids without any staining process.

2.6. Animals. Swiss albino mice (7 to 8 weeks of age, weighing 20−30 g) were obtained and maintained in the Animal house of the AIIMS, New Delhi, under a 12 h light−dark cycle (temperature 24 ± 1 °C, relative humidity 55 ± 10%) and acclimatized for 1 week prior to the experiment with animal feed (Hindustan Pvt. Ltd., India) and water supplied ad libitum. All animal experiments were performed according to the ethical committee of AIIMS, New Delhi, India.

2.7. Preparation of Skin Samples. Male Swiss albino mice skins (25−35 g, 80−90 days old) were used for in vitro permeation studies. After approval from the local ethical committee, animals were obtained from the central animal house facility of All India Institute of Medical Sciences (New Delhi, India). Animals had free access to a pellet diet (Lipton India Ltd.) and water. Abdomen hairs of the mice were removed by applying hair remover cream (Annefrench, Geoffrey Manners & Co., India) 48 h before sacrificing them by cervical dislocation. Subcutaneous fat and connective tissues were removed from intact skin and cheeked through a magnifying glass (×10) and microscope for any damages. Prior to the experiment, skin samples were washed with phosphate buffer saline (PBS, pH of 7.4) solution at room temperature and then the integrity of the skin barrier function was examined by assessing the electric resistance of the skin. Each skin sample was loaded on a Keshary & Chien diffusion cell and allowed for equilibration to a small external charge from a digital multimeter. Ag/AgCl reference electrodes (Bioanalytical Systems Inc., West Lafayette, IN) inserted in the receptor and donor chambers filled with PBS, respectively, was used to examine the electric resistance of the skin.

2.8. Histopathological Observation. For histological examination, skin tissue of Swiss albino mice treated with 200 μL of MTX-RM at W_0 = 5, 10, and 15, respectively, and pure MTX solution in water was used as the control. Skin samples were fixed in 10% buffered formalin (pH 7.4), embedded in paraffin, and processed or histopathological examination. A 3 μm tissue section was cut and stained with routine hematoxylin and eosin for microscopic observations.

2.9. In Vitro MTX Permeation Kinetics. For the in vitro release study of MTX from MTX-RM, a vertical Keshary & Chien diffusion cell was used (volume 18 mL and active area 3.8 cm^2). The hair-depilated mouse skin was mounted at the receptor compartment of the diffusion cell and fixed with rigid clamps. The epidermal layer was equilibrated with the fluid (PBS, pH 7.4) in the receptor compartment with continuous stirring at a constant temperature of 37 ± 0.5 °C with external circulation of water for 45 min. Then, a predetermined dose of MTX-RM was applied on the top of the skin.

For each experiment, 250 μL of MTX-RM containing 100 μg of MTX was applied to the top of the skin, and the samples were collected at a predetermined time. The taken volume of the receptor compartment was refilled with the same amount of the fresh buffer. Quantification of MTX in the receptor compartment of Keshary & Chien diffusion was carried out by a UV−vis spectrophotometer at 302 nm with 1 cm light path length.

2.10. Data Analysis. The steady state skin flux (Jss) of MTX was determined from Fick's law of diffusion (eq 1), and the permeability coefficient (P) was calculated by using eq 2.

$$\text{Jss} = (V/A) \times (dC/dt) \quad (1)$$

$$P = \text{Jss}(\text{CRM})^{-1} \quad (2)$$

whereas Jss is the steady-state skin flux in μg/cm^2/h, V is the volume in mL of receptor compartment, A is the active diffusion area in cm^2, C and CRM are the receptor and initial concentration of MTX in RM, respectively, in mg/mL, and time is in h.

The steady-state skin flux was calculated from the slope of the cumulative amount of MTX in the receptor compartment of the diffusion cell versus the time plot graph using a linear regression method. Statistical analysis was conducted using the student's t-test.

2.11. Visualization of the Skin Penetration and Distribution of the AOT-MTX-Water−Olive Oil Reverse Microemulsion Using CLSM. The skin samples (control, 30 min, and 6 h, treated with MTX-RM, respectively) were fixed in Karnovosk's fixative [2% p-formaldehyde and 1% (w/v) glutaraldehyde] in 0.1 M phosphate buffer (pH 7.4) and processed further. The microtome was used for cutting thin sections of skin and stained with platinum for the field emission scanning electron microscopy (Hitachi S-4700) micrograph. The laser scanning micrographs were obtained using a Bio-Rad make Radiance 2000 Multiphoton Confocal System (equipped with a 650 nm long-pass emission filter). Fluorescence observation was carried out at 488 nm excitation for FITC detection. 100 μL each of 0.05 mM solution of FITC in water as the control was applied on hair depilated mice skin, and for testing samples, 100 μL of MTX-RM (0.05 mM FITC) was applied on another freshly prepared skin. This was followed by blotting freshly prepared skins with inert paper and washing three times with ethanol. The clean samples were trimmed and examined through a confocal microscope in the blue−yellow−red region (488−539 nm range). Micrographs were recorded using a Bio-Rad MRC-1024 confocal laser scanning system (equipped with argon, krypton, and neon laser, Bio-Rads Laboratories) using a 20× water immersion objective lens. The FITC isomer was green, and the background was black.

2.12. Image Analysis. For image analysis, Image-Pro Plus image analysis software (Media Cybernetics' Corporation, USA) was used along with a Research Light Microscope (Model BX50, Olympus Corporation, Japan), 12-bit digital camera (Media Cybernetics' Corporation, USA) with inbuilt

https://doi.org/10.1021/acsomega.3c08875
ACS Omega 2024, 9, 7012−7021

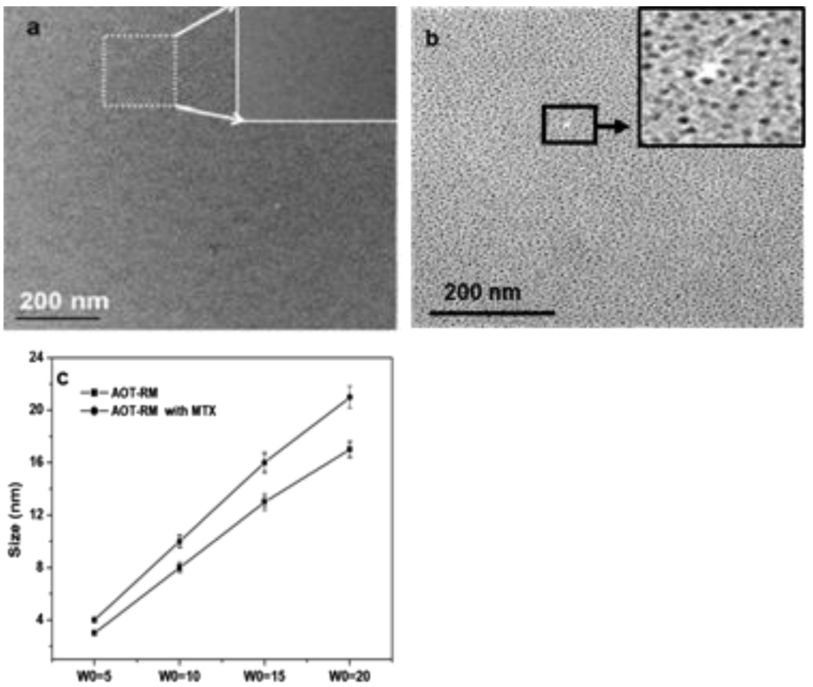

Figure 2. Low-resolution TEM images of (a) AOT-water−OL (AOT-RM) and (b) AOT-MTX-water−OL RM (MTX-RM) at W_0 = 10, respectively, and (c) hydrodynamic size of AOT-RM and MTX-RM at different W_0.

image grabber card, personal computer, and Microsoft Excel software (Microsoft Corporation, USA). In this interactive system, the micrograph was analyzed in the grayscale range. Mean fluorescence intensity of FITC was calculated in a grayscale value inside the epidermis, upper dermis, lower dermis, and skin appendages (such as sweat duct and hair follicles) upon taking into consideration the stability of FITC in AOT microemulsion and water (measured by fluorescence spectrophotometer at λExc: 491 nm and λEm: 518 nm, respectively).

2.13. DSC and ATR/FT-IR Analysis of Treated Swiss Albino Mice Skin. The skin treated with MTX-RM (W_0 = 10) was washed with ethanol to remove any sticking stuff on the surface. Prior to the differential scanning calorimeter (DSC) measurement, 10 mg of the treated skin was freeze-dried for DSC, and those results were recorded on a PerkinElmer DSC-7 instrument (Norwalk, USA) at a heating rate 10 °C/min. Attenuated total reflecting ATR-FT-IR (Shimadzu, Japan) was used to elucidate the interaction of MTX with RM (W_0 = 10) and skin components using the Zinc selenide horizontal cell.

2.14. MTT Cell Viability Assays. The effects of the extracts of MTX-RM on cell proliferation of B16F10 cell lines were determined using MTT cell viability assays, and they were compared with free MTX and MTX unloaded AOT-water−OL RM by reduction of 3-(4,5-dimethylthiazol-2-yl)-2,5-diphenyltetrazolium bromide (MTT) to formazan. B16F10 cells were seeded (2000 cells/well) in 96-well plates; after overnight incubation, cells were treated with varying concentrations of MTX-RM for 72 h or vehicle [0.1% dimethyl sulfoxide (DMSO)]. Then, MTT reagent was added to the medium in each well and incubated for 4 h at 37 °C. Then, reduced formazan crystals were solubilized in DMSO, and optical density values were measured at 540 nm on a microplate reader. All treatments were performed in triplicate, and results were expressed as mean ± SE.

3. RESULTS AND DISCUSSION

3.1. Characterizations of Microemulsion. The scheme for the preparation of AOT-Methotrexate-water−OL RM (MTX-RM) is depicted in Figure 1b and the composition is shown in Table 1. The low-resolution TEM micrograph of freshly prepared MTX-RM with and without MTX at W_0 = 10 is shown in Figure 2. TEM image processing for inverse fast Fourier transformation (IFFT) image analysis was carried out by Digital Micrograph software (version 3.0 manufactured by Gatan Inc.).[30,31]

A loading of MTX in AOT-water−OL RM enhanced the contrast to visualize it without staining by TEM (Figure 2b). The hydrodynamic size of AOT-RM (with and without MTX) increased with the increasing water contents in microemulsion (Figure 2c); also after MTX loading, the size of microemulsion increased, which indicates the MTX loading in AOT-RM. The aging effect on the size of AOT-RM (W_0 = 10) at room temperature and 4 °C is shown in Figure S1a. Hydrodynamic size gradually increased with time at room temperature; however, at 4 °C stored sample, it increased in the first month and then later it was roughly constant for AOT-RM (with and without MTX) (Figure S1a). This is probably due to moisture absorption by the AOT-RM.

The zeta potential of AOT-RM (with and without MTX) is also shown in Table 1. With increasing water content in AOT-RM, a negative zeta potential increased from average −29.42 mV (W_0 = 5) to −35.54 mV (W_0 = 20), and after MTX loading, the decreasing trend was observed (Table 1) which is in correlation with reported work and indication of interaction of MTX with AOT.[32,33] The AOT is an anionic surfactant and double-layer formation in favor of negative charge, and with the increasing water content, many more hydroxy ions are reported in a double layer, and as a result, it shows a more negative zeta potential.[34]

The morphologies of MTX-RM evaluated by a field emission high-resolution transmission electron microscope

https://doi.org/10.1021/acsomega.3c08875
ACS Omega 2024, 9, 7012−7021

(HR-TEM) (FE-TEM, JEOL, JEM-2100, 200 kV) using a low dose electron exposer and nanographs are shown in Figures 3

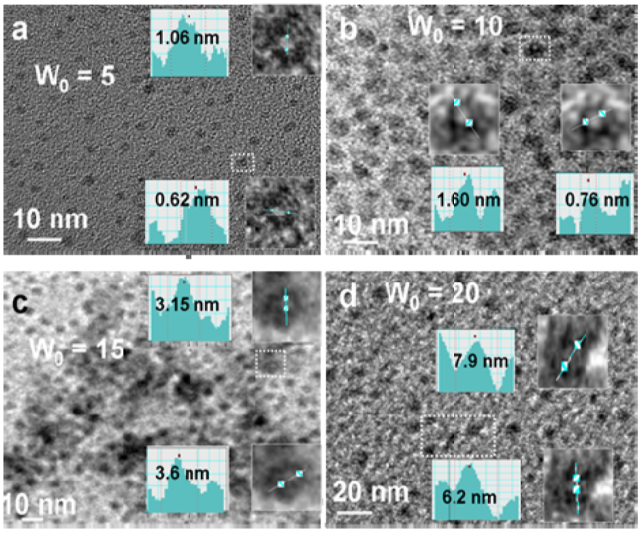

Figure 3. High resolution transmission micrograph (HR-TEM) of AOT-water-MTX-OL RM at W_0 = (a) 5, (b) 10, (c) 15, and (d) 20. Inset figures are the IFFT images of the selected microemulsion of the corresponding highlighted area (marked in box).

and S2. The HR-TEM nanographs of RM at W_0 = 5, 10, 15, and 20 are shown in Figure 3a−d. IFFT images of the highlighted area are shown in the corresponding inset figures. The average thickness of the dark areas at both W_0 = 5 and 10 is 0.65 ± 0.1 nm, which closely matched with the size of the headgroup of AOT (0.54 nm).[35] The dark area at the periphery of the microemulsion (Figure 3) suggests MTX interaction with the headgroup of the AOT, which are in correlation with changing in zeta potential (Table 1). The ellipsoid shape of RM and its core (water droplet) are clearly visible in all inset nanographs.

The average sizes of MTX-RM were calculated from HR-TEM by using the IFFT image [fast Fourier transform (FFT) and IFFT electron microscope nanographs analysis by using Gatan software for the microscope; the FFT data were collected and then converted to IFFT images of the selected area for a better understanding of the nanographs] and diameters of 4 ± 0.8, 7.3 ± 0.8, 12 ± 1.3, and 16 ± 0.9 nm at W_0 values of −5, −10, −15, and −20, respectively. The diameters of the major axis (a) and minor axis (b) of the core at different water contents in RM are also shown in the inserted histogram. The average ratio of the major axis to the minor axis in the core zone of the microemulsion varies from 1.25 ± 0.08 to 2.1 ± 0.1. The eccentricity of the ellipsoid calculated using the following eq 3 was in the range of 0.5−0.87. However, it shows inconsistency with the water content present in the system. At the lower water contents in MTX-RM, the eccentricity was greater than those at higher water contents.

The results of HR-TEM image analysis are in good agreement with previous reports involved with the computational model for AOT microemulsion.[21,22]

$$\text{eccentricity } (e) \text{ of an eclipses} = \sqrt{\{1 - (b^2/a^2)\}} \quad (3)$$

whereas a and b are the diameters of the major and minor axis, respectively.

The effects of storage duration on the shape and size of MTX-RM (W_0 = 10) were evaluated after 1 and 3 months by HR-TEM (Figure S2a,b) and 12 months by AFM (Figure S2c). A dark contrast which is due to MTX also observed inside the core of the RM (Figure S2b); the size of the RM increased from 7.3 ± 0.8 to 25 ± 2 nm as a function of time,

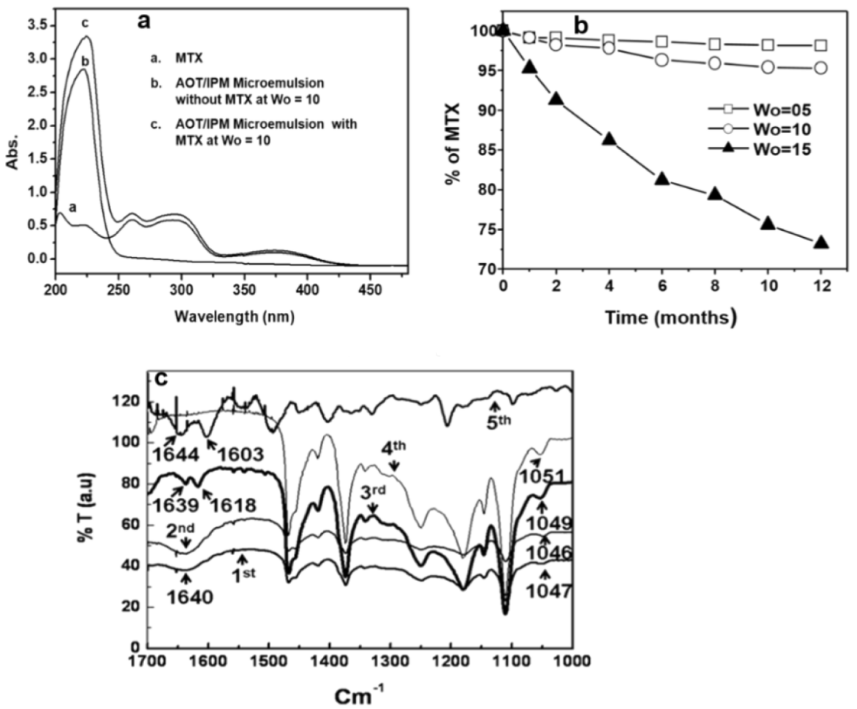

Figure 4. (a) UV−vis spectra; (b) stability of MTX in AOT-water-MTX-OL RM at different water contents, and (c) FT-IR spectra of AOT-MTX-water−OL RM (W_0 = 10) at zero time (1st), 2 months (2nd), and 3 months (3rd). FT-IR spectra of AOT-water−OL (4th) and pure MTX (5th).

https://doi.org/10.1021/acsomega.3c08875
ACS Omega 2024, 9, 7012−7021

and the shape of the microemulsion was transformed from eclipses to wormlike micelles at room temperature.

In order to understand molecules of the MTX in MTX-RM (W_0 = 10), thin film XRD on a silica substrate was carried out. As shown in Figure S2d, the XRD patterns suggest that MTX was encapsulated in RM without affecting the molecular integrity. However; the 2-theta peak at 24.20 (0.37 nm) changed to 23.15 degrees (0.385 nm), and the peak at 39.30 degrees of MTX diminished in MTX-RM (W_0 = 10).[36] This may be due to orientation change and geometrical constraints for MTX in the confined environment of MTX-RM compared with pure MTX.

3.2. Stability of MTX in MTX-RM by UV−vis and FT-IR. The UV−vis scans of pure MTX and AOT-RM in the presence or absence of MTX are shown in Figure 4a, which clearly shows that the carrier peak is not overlaid with MTX picks. The time-bound stability of MTX in MTX-RM at different water contents (W_0 = 5, 10, and 15) at 37 °C was evaluated at an absorbance of 302 nm. As shown in Figure 4b, there was an increase of water content in MTX-RM that subsequently caused a decrease in the stability of MTX as a function of time.[35]

For further confirmation of MTX interaction with AOT head groups, we analyzed samples using FT-IR instruments at the wave range of 4000−400 cm^{-1}. The full range (4000−450 cm^{-1}) FT-IR spectra of AOT-water−OL microemulsion (AOT-RM) in the presence or absence of MTX and OL are shown in Figure S3a−c, respectively. No overlapping of the characteristic peak of MTX in AOT, water, or OL was observed. The FT-IR spectra of pure MTX and AOT-RM (W_0 = 10) in the presence or absence of MTX at varying time intervals are shown in Figure 4c. For FT-IR analysis of MTX in MTX-RM, special attention was placed on the amide peak whose linkage is significantly different between pure MTX and its hydrolysis product. Pure MTX display characteristic amide peaks at 1644 and 1603 cm^{-1} for MTX and its hydrolysis product, respectively (4th spectra of Figure 4c). In MTX-RM (W_0 = 10), these two characteristic peaks of MTX were merged into a broad peak appeared at 1632 cm^{-1} (1st spectra of the Figure 4c).[38]

The merged peak split after 3 months and remained visible for 12 months. The 1644 cm^{-1} peak was red-shifted to 1639 cm^{-1}, while a blue shift was observed for the 1603 cm^{-1} peak (3rd spectra of Figure 4c). No significant change in the alkyl region of the spectrum (3000−2800 cm^{-1}) of MTX-RM was observed. The FT-IR peak of the sulfonic group of the AOT at 1051 cm^{-1} was shifted to 1047 cm^{-1}, which supports the MTX interaction with the headgroup of AOT in MTX-RM.[37] The appearance of the characteristic peak near 3240 cm^{-1} denotes the presence of hydrogen bonding in MTX-RM (Figure S3a).

The nature of the hydrogen bonding networks of the RM is dependent on the water content in it.[39−42] In the RM system, there are bound (interfacial) and free water molecules (which are equilibrated with each other); their presence is dependent on the hydration rate of the system. Six water molecules per SO_3^- group of AOT (up to W_0 = 6) are considered to be rigidly held; thereafter, the rigidity declines up to W_0 = 15 and bulk solvent properties seem to prevail.[43,44]

At low or ambient temperatures, bonded water is less susceptible to phase transitions than bulk water due to the specific structure of the hydrogen bond network within RM, particularly at the interface. MTX is soluble in water at a slightly basic pH and is susceptible to hydrolysis, as shown in Figure 1a. Nevertheless, water in RM is not free to take part in hydrolysis, and as a result, the stability of MTX in MTX-RM (W_0 = 5) is significantly high (~97% viability) at room temperature during the study period of 1 year.

3.3. Toxicological Evaluation. Histopathological results of treated skin are shown in Figure 5. Control groups

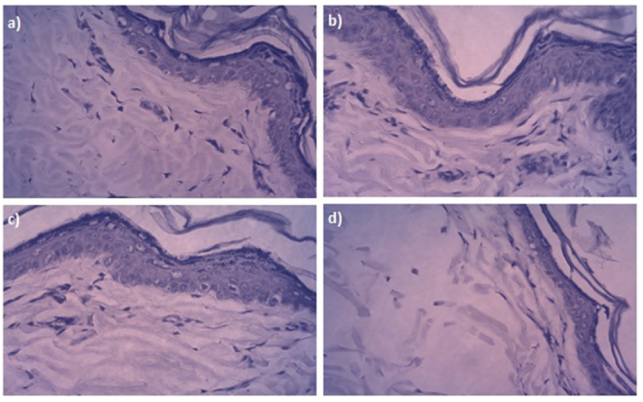

Figure 5. Histopathological microphotographs of different Swiss albino mice groups: (a) control, 0.1 M AOT-MTX-water-−OL RM at (b) W_0 = 5 and (c) W_0 = 10; (d) MTX water solution (400 μg/mL) for 6 h.

presented normal histology of the epidermis and dermis (Figure 5a). MTX-RM at W_0 = 5 presents normal histology and no proliferation of the epidermis (Figure 5b). W_0 = 10 shows no significant proliferation of the epidermis and stratum corneum hyperkeratosis (Figure 5c). An animal group treated with pure MTX solution (pH 7.4) exhibited normal thickening of the epidermis and mild stratum corneum hyperkeratosis (Figure 5d).

3.4. In Vitro Release of MTX by AOT-MTX-Water−Olive Oil Reserve Microemulsion. In vitro skin permeability experiments were carried out on hair-depilated mice skin for release kinetics of MTX from MTX-RM. As shown in Figure 6a, 46.4 ± 14, 56.4 ± 1.3, and 67.6 ± 1.6% of the drug was released to the receptor compartment of the diffusion cell in 6 h for AOT-water-MTX−OL reserve microemulsion at W_0 = 5, W_0 = 10, and W_0 = 15, respectively. The skin flux of MTX was 2.42 ± 0.05, 3.16 ± 0.03, and 3.64 ± 0.09 $\mu g/cm^2/h$ at water contents (W_0) of 5, 10, and 15, respectively, in RM, whereas the sample skin flux of MTX for the control sample is 0.16 ± 0.02 $\mu g/cm^2/h$ (Figure 6b). The skin permeability of MTX achieved about 45-fold enhancement by MTX-RM at W_0 = 15 as compared with the control (MTX aqueous solution) (Figure 6a,b).

3.5. Mechanism of the Skin Permeation. The scanning electron microscopy (SEM) image of water-treated skin (Figure 7a) displays an intact upper dermis. The upper part of the micrograph (Figure 7c) depicts the dispersion of MTX-RM at the surface of the stratum corneum (for a 30 min treatment). As shown in Figure 7e, there was an increase in space between parallel cells of the stratum corneum region (2.3−5.32 μm) of the skin upon treatment of MTX-RM for 6 h. A confocal laser scanning microscopy (CLSM) micrograph of control and FITC-loaded MTX-RM (unloaded FITC was removed by 12 h of dialysis) and treated skin is shown in Figure 7. The major advantage of CLSM is its ability to visualize fluorescent model compounds in tissue without cryo-fixing or embedding.[44,45] Image analysis data show the greater

https://doi.org/10.1021/acsomega.3c08875
ACS Omega 2024, 9, 7012−7021

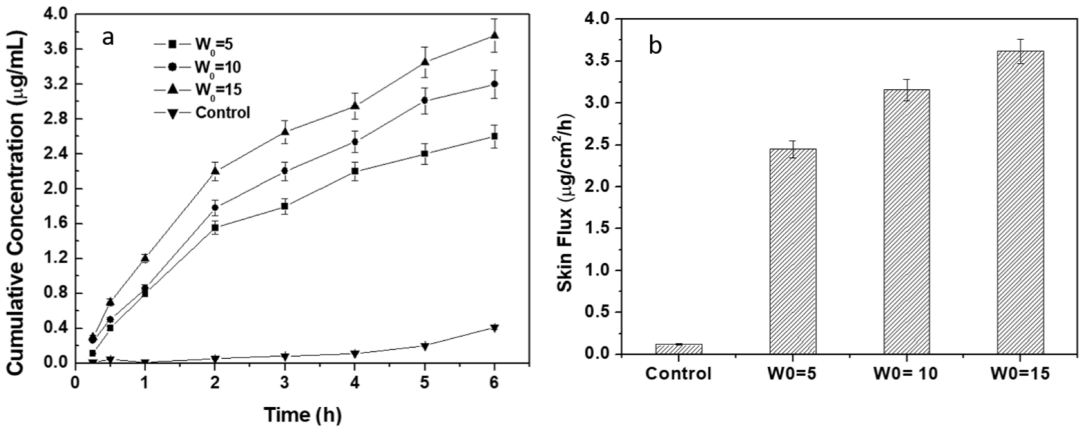

Figure 6. (a) MTX release kinetics and (b) skin flux of MTX from AOT-MTX-water−OL RM at different water contents through mice skin at 37 °C (control is an aqueous solution of MTX).

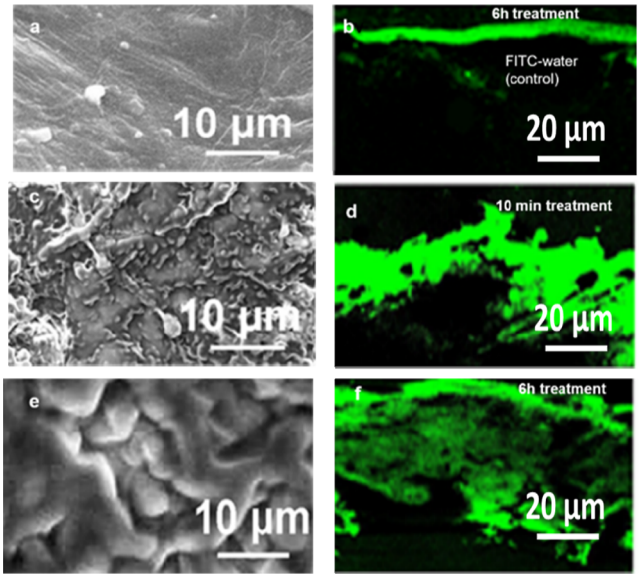

Figure 7. (a) Scanning electron microscopy (SEM) micrograph of Swiss albino mice skin after treatment with (a) water for 6 h and (b) FITC-water, (c) SEM image of treated skin with AOT-water-FITC-OL reverse microemulsion (W_0 = 10) for 10 min and (d) CLSM of 10 min treated skin with AOT-water-FITC-OL RM (W_0 = 10), (e) SEM image of treated skin with AOT-water-FITC-OL RM (W_0 = 10) for 6 h, and (f) CLSM of 6 h treated skin with AOT-water-FITC-OL RM (W_0 = 10).

deposition of the fluorescent level only at the superficial levels of the stratum corneum being treated with the control formulation (FITC-water solution) for 6 h (Figure 7b). As shown in Figure 7d,f, the permeation rate of FITC in stratum corneum, epidermis, and dermis depends on the duration of treatment. There was significantly enhanced fluorescence intensity from the stratum corneum, hair follicles, sweat gland, epidermis, and dermis layer after exposure for 10 min as compared with the control (Figure 7d). The highest intensity of fluorescent FITC was observed in deeper layers of the dermis for 6 h-treated skin (Figure 7f). The MTX-RM were able to uniformly diffuse into the dermis to a great extent after being exposed for 6 h.

In continuous studies, differential calorimeter analysis and ATR/FT-IR on treated mice skin were conducted. As shown in Figure S4, skin treated with MTX-RM for 6 h displayed a broad new transition at 50−95 °C. In normal mouse skin, three main thermal transitions are around 65 °C (T_2), 82 °C (T_3), and 95 °C (T_4); T_2 and T_3 transitions are associated with lipid phase changes in the intercellular bilayer of the skin, whereas T_4 transition was associated with denaturation of protein.[13,15]

Skin has multicomponent layers with an unique structure and function: the epidermis, the dermal-epidermal junction, the dermis, and the hypodermis.[46] Infrared light can penetrate up to 20 μm depth in the skin.[47] The epidermis mainly gives a vibrational spectrum of amide I and amide II protein bands at 1650 and 1550 cm^{-1}, respectively, due to keratinocytes of the epithelial component. Amide I arises from hydrogen-bonded C═O stretching vibrations and amide II from C−N stretching and CNH bending vibrations. The FT-IR peak of the dermis region dominated by fibrous type I collagen and hypodermis is dominated by the presence of lipids, with characteristic CH_2 and CH_3 symmetric and asymmetric stretching modes in the 2800−3100 cm^{-1} range and carbonyl (C═O) stretching vibrations of ester bonds in membrane phospholipids near 1750 cm^{-1}.[48] Figure 8 represents ATR/FT-IR spectra of MTX-RM, untreated skin, and 6 h treated skin with MTX-RM. For characterization of treated skin by ATR, the carbonyl peak of the lipid ester group, amide 1, amide 2 peak of the proteins, and carbohydrate (1150−1025 cm^{-1}) either from glycolipid, glycoprotein, or glycosamine are analyzed because hydrocarbon chains are also present in OL and AOT (Figure 1).

The carbonyl peak of the ester group (lipid) for the control skin sample appeared at 1742 cm^{-1} (Figure 8a), that of microemulsion appeared at 1751 cm^{-1}, as shown in Figure S3a, and that of microemulsion-treated samples of the skin appeared at 1736 cm^{-1} (Figure 8b,c). A sulfonic group of the AOT gave a peak at 1051 cm^{-1} (Figure 4c; fourth spectra without MTX) and 1046 cm^{-1} (Figure 4c; first spectra with MTX); it shows a sharp peak near 1065 cm^{-1} in treated skin, which was diverted from the control sample (Figure 8b,c). Also, the changes in the amide II band were observed in treated skin as compared to the control skin (near 1550 cm^{-1}), indicating that the sulfonic headgroup of the AOT microemulsion plays an integral role in defining the permeation profiles of the MTX-RM through the skin. The peak at 1240 and 1075 cm^{-1} represents asymmetric and symmetric stretching, respectively, of PO^{2-}. The carbohydrate peaks in the range of 1025−1045 cm^{-1} are related to the vibrational modes of $-CH_2OH$ groups, C−O stretching, and C−O

https://doi.org/10.1021/acsomega.3c08875
ACS Omega 2024, 9, 7012−7021

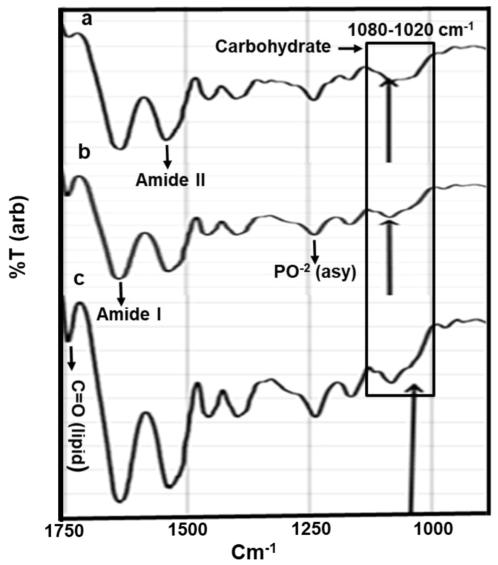

Figure 8. (a) ATR/FT-IR spectra of (b) untreated hair-depilated Swiss albino mice skin, (c) 6 h treated skin with AOT-MTX-Water−OL RM at W_0 = 5, and (c) 6 h treated skin with AOT-MTX-Water−OL RM at W_0 = 10.

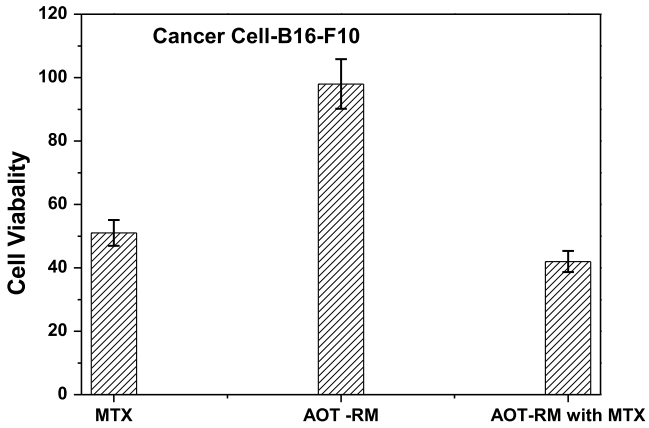

Figure 9. Comparison of B-16-F10 melanoma cell viability after treatment for 72 h.

bending of the C−OH groups. ATR data show that MTX-RM carrier interacts with the carbohydrate −C−OH group (1060−1020 cm^{-1}) of the glycolipid and glycoprotein (Figure 8).[49−51]

As the transition from an amorphous solid to a crystalline solid produces a peak in the DSC signal, a broad peak near 74 °C could be a combination of T_2, T_3, and T_4 peaks. A broadening of this endothermic transition seems to be due to encapsulation of AOT microemulsion into the intercellular regions of the skin and denaturalization of protein via interaction of an anionic headgroup of the AOT with skin components as observed, and it can be correlated with the confocal laser scanning micrograph (Figure 7d,f) and ATR/FT-IR spectra (Figure 8) of MTX-RM treated Swiss albino mice skin. There is the interaction of RM with the skin components, enhancing the movement in intercellular lipid and protein domains of the treated skin and perturbing its architecture for permeation.[52−56]

The extent of perturbation in the stratum corneum depends on the content of water in RM. As the water content increases in RM, the disordering of lipid layers increases, leading to an increase in motional freedom of the lipid hydrocarbon chain, the fluidity in the stratum corneum of the skin, and interaction with protein probably through hydrogen bonding and sulfonic group of the AOT.[54] Also, the possibility of diffusion during permeation MTX cannot be ruled out because sizes of MTX-RM are smaller than the mammalian cell pore that facilitates diffusion through the pore of the stratum corneum and appendage (Figure 7d,f, respectively), which may be the main reason for drug permeation in the beginning.[10,12,55−57]

3.6. MTT Test. To be a viable drug delivery system, a loaded carrier system must show that it can deliver the agents into the cell. Second, the loaded particles should show a better efficacy than the free drugs. To test these measures for MTX-RM, we compared the cell viability for treated cells with AOT-RM and cells treated with pure MTX-water solution. Figure 9 shows that cells treated with AOT-RM were almost completely viable, as opposed to the cells treated with MTX-RM. It indicates that the carrier itself is not active against the B-16-F10 melanoma cell. Furthermore, Figure 9 indicates that MTX-RM shows a better efficacy than free MTX for B-16-F10 melanoma cells.

The MTX-RM due to the negative charge headgroup of the AOT interact with cell membrane glycolipid and protein for permeation and can entrap and interact with endosomes or lysosomes present in the cell, leading to the release of MTX.[53−58]

4. CONCLUSIONS

The interaction of MTX with the AOT headgroup offers a unique property of direct revelation of the shape and size of the core and periphery of the microemulsion. The effects of pH on the stability of MTX at W_0 = 5 and 10 were negligible, supporting the fact that orientation/geometrical constraint on MTX amide linkage plays an integral role in the stability of MTX. In vitro release profiles of MTX from MTX-RM at W_0 values of 5, 10, and 15 displayed 15.5-, 17.2-, and 21.7-fold enhancement, respectively, in the skin flux compared with the control formulation. MTX from the FITC-loaded AOT-MTX-water−OL reserve microemulsion was detected at hair follicles, sweat glands, and epidermis layer of the treated skin by CLSM. Cell viability data suggested that carrier AOT-water−OL reserve microemulsion does not affect the viability of the B-16-F10 melanoma cell. In conclusion, AOT-water−OL reserve microemulsion facilitates penetration of MTX through the skin, providing its effective accumulation in the deeper layers of dermis. A confined environment of an RM could be used as a stabilizing means for chemically unstable pharmaceutically active molecules, which are susceptible to the hydrolysis process.

■ ASSOCIATED CONTENT

Supporting Information

The Supporting Information is available free of charge at https://pubs.acs.org/doi/10.1021/acsomega.3c08875.

Time- and temperature-dependent size analysis of MTX-RM by DLS, IFFT images (TEM), atomic force micrograph, thin film XRD of MTX-RM, and DSC thermogram of Swiss albino control and treated skin with MTX-RM (PDF)

https://doi.org/10.1021/acsomega.3c08875
ACS Omega 2024, 9, 7012−7021

AUTHOR INFORMATION

Corresponding Author

Mohammad Changez − *College of Health Science, University of Buraimi, Al Buraimi 512, Oman;* orcid.org/0000-0001-5304-8962; Email: mchangez@uob.edu.om

Authors

Mohammad Faiyaz Anwar − *Department of Microbiology, All Indian Institute of Medical Sciences AIIMS, New Delhi 110608, India*

Hilal Alrahbi − *College of Health Science, University of Buraimi, Al Buraimi 512, Oman*

Complete contact information is available at: https://pubs.acs.org/10.1021/acsomega.3c08875

Author Contributions

M.C. and M.F.A. designed experiments and wrote manuscript; M.F.A. carried out FT-IR, DSC, TEM, AFM, XRD, and histopathology and MTT experiments. M.C. supported M.F.A. in analyzing FT-IR/ATR, DSC, and TEM data. H.A. prepared samples for the in vitro experiment and histopathology. H.A. was involved in text editing.

Funding

This research leading to these results has received funding from Ministry of Higher Education, Research and Innovation (MoHERI) of the Sultanate of Oman under Bulk Funding Program with Agreement Number MoHERI/BFP/UOB/RG01/2022.

Notes

The authors declare no competing financial interest.

ACKNOWLEDGMENTS

M.C. and H.A. thank the Ministry of Higher Education, Research, and Innovation (MoHERI) of the Sultanate of Oman for providing funds and also thank the management team of University of Buraimi for logistic support. M.C. also thanks Korean Basic Institute, Daejon, South Korea for HR-TEM and AFM analysis.

ABBREVIATIONS

MTX, methotrexate (4-amino-10-methylfolic acid or 4-amino-4-deoxy-10- methylpteroyl-L-glutamicacid); AOT, sodium bis(2-ethyl hexyl) sulfosuccinate; OL, olive oil; UV−vis, ultraviolet−visible; FT-IR, Fourier transform-infrared; DSC, differential scanning calorimeter; AFM, atomic force microscope; SEM, scanning electron microscope; TEM, transmission electron microscope; XRD, X-ray diffraction; RM, reverse microemulsion

REFERENCES

(1) Kompis, I. M.; Islam, K.; Then, R. L. DNA and RNA Synthesis: Antifolates. *Chem. Rev.* **2005**, *105*, 593−620.

(2) Hu, J.; Bian, Q.; Ma, X.; Xu, Y.; Gao, J. A double-edged sword: ROS related therapies in the treatment of psoriasis. *Asian J. Pharm. Sci.* **2022**, *17*, 798−816.

(3) Choi, G.; Kim, T.-H.; Oh, J.-M.; Choy, J.-H. Emerging nanomaterials with advanced drug delivery functions; focused on methotrexate delivery. *Coord. Chem. Rev.* **2018**, *359*, 32−51.

(4) Sunoqrot, S.; Mahmoud, N. N.; Ibrahim, L. H.; Al-Dabash, S.; Raschke, H.; Hergenröder, R. Tuning the Surface Chemistry of Melanin-Mimetic Polydopamine Nanoparticles Drastically Enhances Their Accumulation into Excised Human Skin. *ACS Biomater. Sci. Eng.* **2020**, *6*, 4424−4432.

(5) Nissen, K. B.; Jorgensen, L. B.; Berg, D. L.; Andersen, G. Stability study of methotrexate in 0.9% sodium chloride injection and 5% dextrose injection with limit tests for impurities. *Am. J. Health-Syst. Pharm.* **2017**, *74* (9), e211−e223.

(6) Ray, S.; Joy, M.; Sa, B.; Ghosh, S.; Chakraborty, J. pH dependent chemical stability and release of methotrexate from a novel nanoceramic carrier. *RSC Adv.* **2015**, *5*, 39482−39494.

(7) Vrignaud, S.; Briot, T.; Launay, A.; Kempf, M.; Lagarce, F. Design and stability study of a paediatric oral solution of methotrexate 2mg/ml. *Int. J. Pharm.* **2015**, *487*, 270−273.

(8) Prow, T. W.; Grice, J. E.; Lin, L. L.; Faye, R.; Butler, M.; Becker, W.; Wurm, E. M. T.; Yoong, C.; Robertson, T. A.; Soyer, H. P.; Roberts, M. S. Nanoparticles and microparticles for skin drug delivery. *Adv. Drug Delivery Rev.* **2011**, *63*, 470−491.

(9) Chen, Y.; Liao, M.; Ma, K.; Wang, Z.; Demé, B.; Penfold, J.; Lu, J. R.; R. P. Webster, J.; Li, P. Implications of surfactant hydrophobic chain architecture on the Surfactant-Skin lipid model interaction. *J. Colloid Interface Sci.* **2022**, *608*, 405−415.

(10) Spernath, A.; Aserin, A.; Sintov, A. C.; Garti, N. Phosphatidylcholine embedded micellar systems: Enhanced permeability through rat skin. *J. Colloid Interface Sci.* **2008**, *318* (2), 421−429.

(11) Ali, M. K.; Moshikur, R. M.; Wakabayashi, R.; Moniruzzaman, M.; Goto, M. Biocompatible Ionic Liquid-Mediated Micelles for Enhanced Transdermal Delivery of Paclitaxel. *ACS Appl. Mater. Interfaces* **2021**, *13*, 19745−19755.

(12) Shah, J.; Nair, A. B.; Shah, H.; Jacob, S.; Shehata, T. M.; Morsy, M. A. Enhancement in antinociceptive and anti-inflammatory effects of tramadol by transdermal proniosome gel. *Asian J. Pharm. Sci.* **2020**, *15*, 786−796.

(13) Changez, M.; Varshney, M.; Chander, J.; Dinda, A. K. Effect of the composition of lecithin/n-propanol/isopropyl myristate/water microemulsions on barrier properties of mice skin for transdermal permeation of tetracaine hydrochloride: in vitro. *Colloids Surf., B* **2006**, *50*, 18−25.

(14) Hathout, R. M.; Mansour, S.; Geneidi, A. S.; Mortada, N. D. Visualization, dermatopharmacokinetic analysis and monitoring the conformational effects of a microemulsion formulation in the skin stratum corneum. *J. Colloid Interface Sci.* **2011**, *354*, 124−130.

(15) Lawrence, M. J.; Rees, G. D. Microemulsion-based media as novel drug delivery systems. *Adv. Drug Delivery Rev.* **2000**, *45*, 89−121.

(16) Huang, Z.; Wu, H.; Yang, B.; Chen, L.; Huang, Y.; Quan, G.; Zhu, C.; Li, X.; Pan, X.; Wu, C. Anhydrous reverse micelle nanoparticles: new strategy to overcome sedimentation instability of peptide-containing pressurized metered-dose inhalers. *Drug Delivery* **2017**, *24*, 527−538.

(17) Chowdhary, J.; Ladanyi, B. M. Molecular Simulation Study of Water Mobility in Aerosol-OT Reverse Micelles. *J. Phys. Chem. A* **2011**, *115*, 6306−6316.

(18) Abel, S.; Sterpone, F.; Bandyopadhyay, S.; Marchi, M. Molecular modeling and simulations of AOT-water reverse micelles in isooctane: structural and dynamic properties. *J. Phys. Chem. B* **2004**, *108*, 19458−19466.

(19) Baruah, B.; Roden, J. M.; Sedgwick, M.; Correa, N. M.; Crans, D. C.; Levinger, N. E. When is water not water? Exploring water confined in large reverse micelles using a highly charged inorganic molecular probe. *J. Am. Chem. Soc.* **2006**, *128*, 12758−12765.

(20) Fuglestad, B.; Gupta, K.; Wand, A. J.; Sharp, K. A. Characterization of Cetyltrimethylammonium Bromide/Hexanol Reverse Micelles by Experimentally Benchmarked Molecular Dynamics Simulations. *Langmuir* **2016**, *32*, 1674−1684.

(21) Abel, S.; Waks, M.; Urbach, W.; Marchi, M. Structure, Stability, and Hydration of a Polypeptide in AOT Reverse Micelles. *J. Am. Chem. Soc.* **2006**, *128*, 382−383.

(22) Senske, M.; Smith, A. E.; Pielak, G. J. Protein Stability in Reverse Micelles. *Angew. Chem.* **2016**, *128* (11), 3650−3653.

(23) Castro-Quezada, I.; Román-Viñas, B.; Serra-Majem, L. The Mediterranean diet and nutritional adequacy: a review. *Nutrients* **2014**, *6*, 231−248.
(24) Papadimitriou, V.; Tzika, E. D.; Pispas, S.; Sotiroudis, T. G.; Xenakis, A. Microemulsions based on virgin olive oil: A model biomimetic system for studying native oxidative enzymatic activities. *Colloids Surf., A* **2011**, *382*, 232−237.
(25) Zhang, J.; Han, B.; Liu, J.; Zhang, X.; Yang, G.; He, J.; Liu, Z.; Jiang, T.; Wang, J.; Dong, B. Effect of compressed CO_2 on the size and stability of reverse micelles: Small-angle x-ray scattering and phase behavior study. *J. Chem. Phys.* **2003**, *118*, 3329−3333.
(26) Takeda, J.; Iwao, Y.; Karashima, M.; Yamamoto, K.; Ikeda, Y. Structural Evaluation of the Choline and Geranic Acid/Water Complex by SAXS and NMR Analyses. *ACS Biomater. Sci. Eng.* **2021**, *7*, 595−604.
(27) Mills, A. J.; Wilkie, J.; Britton, M. M. NMR and Molecular Dynamics Study of the Size, Shape, and Composition of Reverse Micelles in a Cetyltrimethylammonium Bromide (CTAB)/n-Hexane/Pentanol/Water Microemulsion. *J. Phys. Chem. B* **2014**, *118*, 10767−10775.
(28) Piletic, I. R.; Moilanen, D. E.; Levinger, N. E.; Fayer, M. D. What nonlinear-IR experiments can tell you about water that the IR spectrum cannot. *J. Am. Chem. Soc.* **2006**, *128*, 10366−10367.
(29) Boyd, J. E.; Briskman, A.; Sayes, C. M.; Mittleman, D.; Colvin, V. Terahertz vibrational modes of inverse micelles. *J. Phys. Chem. B* **2002**, *106*, 6346−6353.
(30) Hensel, J. K.; Carpenter, A. P.; Ciszewski, R. K.; Schabes, B. K.; Kittredge, C. T.; Moore, F. G.; Richmond, G. L. Molecular characterization of water and surfactant AOT at nano emulsion surfaces. *Proc. Natl. Acad. Sci. U.S.A.* **2017**, *114*, 13351−13356.
(31) Fathi, M.; Barar, J.; Erfan-Niya, H.; Omidi, Y. Methotrexate-conjugated chitosan-grafted pH- and thermo-responsive magnetic nanoparticles for targeted therapy of ovarian cancer. *Int. J. Biol. Macromol.* **2020**, *154*, 1175−1184.
(32) Cao, H.; An, B.; Wang, Y.; Zhou, K.; Lu, N. Investigation of Surfactant AOT Mediated Charging of PS Particles Dispersed in Aqueous Solutions. *Coatings* **2019**, *9*, 471.
(33) Zhang, Y.; Zhuo, R. X. Synthesis and drug release behavior of poly (trimethylene carbonate)-poly (ethylene glycol)-poly (trimethylene carbonate) nanoparticles. *Biomaterials* **2005**, *26*, 2089−2094.
(34) Chai, D.; Hao, B.; Hu, R.; Zhang, F.; Yan, J.; Sun, Y.; Huang, X.; Zhang, Q.; Jiang, H. Delivery of Oridonin and Methotrexate via PEGylated Graphene Oxide. *ACS Appl. Mater. Interfaces* **2019**, *11*, 22915−22924.
(35) Simmons, B. A.; Taylor, C. E.; Landis, F. A.; John, V. T.; McPherson, G. L.; Schwartz, D. K.; Moore, R. Microstructure determination of AOT+ phenol organogels utilizing small-angle X-ray scattering and atomic force microscopy. *J. Am. Chem. Soc.* **2001**, *123*, 2414−2421.
(36) Khodashenas, B.; Ardjmand, M.; Rad, A. S.; Esfahani, M. R. Gelatin-coated gold nanoparticles as an effective pH-sensitive methotrexate drug delivery system for breast cancer treatment. *Mater. Today Chem.* **2021**, *20*, 100474.
(37) Giammona, G.; Goffredi, F.; Turco Liveri, V.; Vassallo, G. Water structure in water/AOT/n-heptane microemulsions by FT-IR spectroscopy. *J. Colloid Interface Sci.* **1992**, *154*, 411−415.
(38) Kohler, N.; Sun, C.; Wang, J.; Zhang, M. Methotrexate-modified superparamagnetic nanoparticles and their intracellular uptake into human cancer cells. *Langmuir* **2005**, *21*, 8858−8864.
(39) Bellissent-Funel, M.-C.; Hassanali, A.; Havenith, M.; Henchman, R.; Pohl, P.; Sterpone, F.; van der Spoel, D.; Xu, Y.; Garcia, A. E. Water Determines the Structure and Dynamics of Proteins. *Chem. Rev.* **2016**, *116*, 7673−7697.
(40) Levinger, N. E. Water in confinement. *Science* **2002**, *298*, 1722−1723.
(41) Eskici, G.; Axelsen, P. H. The Size of AOT Reverse Micelles. *J. Phys. Chem. B* **2016**, *120*, 11337−11347.
(42) Simorellis, A. K.; Van Horn, W. D.; Flynn, P. F. Dynamics of low temperature induced water shedding from AOT reverse micelles. *J. Am. Chem. Soc.* **2006**, *128*, 5082−5090.
(43) Vinardell, M. P.; Mitjans, M. Alternative methods for eye and skin irritation tests: An overview. *J. Pharm. Sci.* **2008**, *97*, 46−59.
(44) Changez, M.; Chander, J.; Dinda, A. K. Transdermal permeation of tetracaine hydrochloride by lecithin microemulsion: in vivo. *Colloids Surf., B* **2006**, *48*, 58−66.
(45) Zhang, D.; Bian, Q.; Zhou, Y.; Huang, Q.; Gao, J. The application of label-free imaging technologies in transdermal research for deeper mechanism revealing. *Asian J. Pharm. Sci.* **2021**, *16*, 265−279.
(46) Barth, A.; Zscherp, C. What vibrations tell about proteins. *Q. Rev. Biophys.* **2002**, *35*, 369−430.
(47) Brancaleon, L.; Bamberg, M. P.; Sakamaki, T.; Kollias, N. Attenuated Total Reflection−Fourier Transform Infrared Spectroscopy as a Possible Method to Investigate Biophysical Parameters of Stratum Corneum In Vivo. *J. Invest. Dermatol.* **2001**, *116*, 380−386.
(48) Kyriakidou, M.; Mavrogenis, A. F.; Kyriazis, S.; Markouizou, A.; Theophanides, T.; Anastassopoulou, J. An FT-IR spectral analysis of the effects of γ-radiation on normal and cancerous cartilage. *In Vivo* **2016**, *30*, 599−604.
(49) Kyriakidou, M.; Anastassopoulou, J.; Tsakkiris, A.; Koul, M.; Theophanides, T. FT-IR Spectroscopy Study in Early Diagnosis of Skin Cancer. *In Vivo* **2017**, *31*, 1131−1137.
(50) Cestelli Guidi, M.; Mirri, C.; Fratini, E.; Licursi, V.; Negri, R.; Marcelli, A.; Amendola, R. In vivo skin leptin modulation after 14 MeV neutron irradiation: a molecular and FT-IR spectroscopic study. *Anal. Bioanal. Chem.* **2012**, *404*, 1317−1326.
(51) Altamimi, M. A.; Hussain, A.; Mahdi, W. A.; Imam, S. S.; Alshammari, M. A.; Alshehri, S.; Khan, M. R. Mechanistic Insights into Luteolin-Loaded Elastic Liposomes for Transdermal Delivery: HSPiP Predictive Parameters and Instrument-Based Evidence. *ACS Omega* **2022**, *7*, 48202−48214.
(52) Fu, Y.; Liu, P.; Chen, M.; Jin, T.; Wu, H.; Hei, M.; Wang, C.; Xu, Y.; Qian, X.; Zhu, W. On-demand transdermal insulin delivery system for type 1 diabetes therapy with no hypoglycemia risks. *J. Colloid Interface Sci.* **2022**, *605*, 582−591.
(53) Jindal, A. B. The effect of particle shape on cellular interaction and drug delivery applications of micro- and nanoparticles. *Int. J. Pharm.* **2017**, *532*, 450−465.
(54) Dumoga, S.; Rai, Y.; Bhatt, A. N.; Tiwari, A. K.; Singh, S.; Mishra, A. K.; Kakkar, D. Block Copolymer Based Nanoparticles for Theranostic Intervention of Cervical Cancer: Synthesis, Pharmacokinetics, and in Vitro/in Vivo Evaluation in HeLa Xenograft Models. *ACS Appl. Mater. Interfaces* **2017**, *9*, 22195−22211.
(55) Yang, M.; Meng, J.; Han, L.; Yu, X.; Fan, Z.; Yuan, Y. Pharmacokinetic Study of Triptolide Nanocarrier in Transdermal Drug Delivery System-Combination of Experiment and Mathematical Modeling. *Molecules* **2023**, *28*, 553.
(56) Rippe, B.; Rosengren, B. I.; Carlsson, O.; Venturoli, D. Transendothelial transport: the vesicle controversy. *J. Vasc. Res.* **2002**, *39*, 375−390.
(57) Chen, X.; Wang, Y.; Cheng, Z.; Wei, J.; Shi, Y.; Qian, J. Diffusion Behavior of Drug Molecules in Acrylic Pressure-Sensitive Adhesive. *ACS Omega* **2020**, *5*, 9408−9419.
(58) Kou, L.; Sun, J.; Zhai, Y.; He, Z. The endocytosis and intracellular fate of nanomedicines: Implication for rational design. *Asian J. Pharm. Sci.* **2013**, *8*, 1−10.

https://doi.org/10.1021/acsomega.3c08875
ACS Omega 2024, 9, 7012−7021